Low-lying dipole response of ^{64}Ni

M. Müscher,[1,*] E. Litvinova,[2,3,4] R. Schwengner,[5] T. Beck,[3] D. Bemmerer,[5] F. Fiedler,[5] S. W. Finch,[6,7] U. Friman-Gayer,[8] S. Hammer,[5] J. Isaak,[9] R. V. F. Janssens,[7,10] A. R. Junghans,[5] N. Kelly,[11] F. Kluwig,[1] Krishichayan,[6,7] S. E. Müller,[5] O. Papst,[9] K. Römer,[5] D. Savran,[12] M. Scheck,[11] T. Schüttler,[1] J. Sinclair,[11,13] T. Szücs,[5,†] W. Tornow,[6,7] A. Wagner,[5] J. Wilhelmy,[1] and A. Zilges[1]

[1] *Universität zu Köln, Institut für Kernphysik, 50937 Köln, Germany*
[2] *Department of Physics, Western Michigan University, Kalamazoo, MI 49008, USA*
[3] *Facility for Rare Isotope Beams, Michigan State University, East Lansing, MI 48824, USA*
[4] *GANIL, CEA/DRF-CNRS/IN2P3, F-14076 Caen, France*
[5] *Helmholtz-Zentrum Dresden-Rossendorf, 01328 Dresden, Germany*
[6] *Department of Physics, Duke University, Durham, North Carolina 27708, USA*
[7] *Triangle Universities Nuclear Laboratory, Durham, North Carolina 27708, USA*
[8] *European Spallation Source ERIC, 22484 Lund, Sweden*
[9] *Institut für Kernphysik, Technische Universität Darmstadt, 64289 Darmstadt, Germany*
[10] *Department of Physics and Astronomy, University of North Carolina at Chapel Hill, Chapel Hill, North Carolina 27599, USA*
[11] *School of Computing, Engineering, and Physical Sciences, University of the West of Scotland, Paisley PA1 2BE, United Kingdom*
[12] *GSI Helmholtzzentrum für Schwerionenforschung GmbH, 64291 Darmstadt, Germany*
[13] *SUPA, Scottish Universities Physics Alliance, United Kingdom*

(Dated: March 19, 2024)

Two complementary real-photon scattering experiments were conducted on the proton-magic ^{64}Ni nucleus to study the dipole response up to its neutron-separation energy of $S_n = 9.7\,\mathrm{MeV}$. By combining both measurements, 87 $E1$ and 23 $M1$ transitions were identified above 4.3 MeV. The results of the observed $M1$ transitions were compared to shell-model calculations using two different model spaces. It was found that the inclusion of excitations across the $Z = 28$ shell gap in the calculations has a large impact. Furthermore, average cross sections for decays to the ground state (elastic transitions) as well as to lower-lying excited states (inelastic decays) were determined. The corresponding $E1$ channel was compared to calculations within the relativistic equation of motion (REOM) framework. Whereas the calculations of highest possible complexity reproduce the fragmentation and overall behavior of the $E1$ average elastic cross section well, the predicted absolute cross sections are approximately twice as high as the experimental upper limits even though the latter also include an estimate of the inelastic-decay channel.

I. INTRODUCTION

For decades, the investigation of the low-lying dipole response of atomic nuclei has been a topic of great interest. Especially, the accumulation of electric dipole ($E1$) strength on top of the low-energy tail of the IsoVector Giant Dipole Resonance (IVGDR) [1], commonly denoted as the Pygmy Dipole Resonance (PDR), has attracted a lot of attention [2–4]. Nevertheless, some open questions concerning this $E1$ excitation mode remain, including its microscopic structure and its origin.

Systematic studies of the PDR are one approach for achieving a better understanding. On the one hand, these can be performed along isotopic and isotonic chains to investigate the influence of changes in, e.g., shell structures, neutron excess, and deformation. Such studies were performed, e.g., on the $N = 82$ isotonic chain [5–11] and the $Z = 50$ isotopes [12–16] using real-photon scattering experiments.

On the other hand, comparisons between the observed electric dipole response induced in various nuclear reactions can be a testing ground for the excitation mechanism (see, e.g., Refs. [14, 17, 18]). These studies become difficult if a non-negligible contribution of $M1$ strength - likely stemming from spin-flip resonances - is also located close to the neutron-separation energy S_n. This is the case, e.g., in nuclei close to the $N = 28$ or $Z = 28$ shells, such as ^{54,56}Fe [19, 20] and ^{58,60}Ni [21–23]. In these nuclei, a considerable magnetic dipole ($M1$) contribution was observed in ($\vec{\gamma}$,γ') measurements with a polarized photon beam. Thus, especially for these nuclei, a clear distinction between $E1$ and $M1$ contributions is crucial. Two complementary (γ, γ') experiments on the proton-magic $Z = 28$ nucleus ^{64}Ni were performed to expand the investigations of the dipole response in medium-mass nuclei. Real-photon scattering measurements have already been performed on the two lightest stable, even-even Ni isotopes ^{58,60}Ni up to 10 MeV [21–23] and the $N = 36$ isotone ^{66}Zn up to the neutron-separation energy $S_n = 11.1\,\mathrm{MeV}$ [24, 25]. The combination of complementary (γ, γ') experiments using bremsstrahlung as well as polarized quasimonoenergetic photon beams from Laser-Compton-Backscattering (LCB) enabled the clear identification of the observed transitions and the determination of absolute physical quantities.

This article starts with a short introduction to real-

* muescher@ikp.uni-koeln.de
† Present address: Institute for Nuclear Research (Atomki), 4001 Debrecen, Hungary

photon scattering experiments and continues with descriptions of the experiments and the analysis techniques. Finally, the experimental results for the $E1$ channel are compared to calculations in the equation of motion (EOM) framework, and the $M1$ ground-state transitions of resolved states are discussed with respect to shell-model calculations.

II. NUCLEAR RESONANCE FLUORESCENCE METHOD

The Nuclear Resonance Fluorescence (NRF) method is based on real-photon scattering [26–28]. Real photons predominantly induce dipole, and with a lower probability, also quadrupole transitions from the ground state because they can only transfer small angular momenta. The deexcitation of the photoexcited state can either happen directly back to the ground state by the emission of a single photon (elastic transition), or via intermediate states and, subsequently, back to the ground state by emitting more than one γ ray (inelastic transition). Because real photons are used in the entrance and in the exit channel, many quantities can be extracted in a model-independent way. In this section only a short introduction to the formalism of NRF based on Refs.[26–28] is given. For further information, the reader is referred to these review articles.

II.1. State-to-state analysis

One measure for the probability that a certain transition occurs, which can directly be extracted from NRF experiments, is the so-called energy-integrated cross section I_S. It is calculated by correcting the number of recorded events at the respective γ-ray energy E_γ, i.e., the integrated peak area A in the deexcitation spectrum, for the number of target nuclei N_T, the number of incident photons per energy and area at the corresponding excitation energy $N_\gamma(E_x)$, the detection efficiency $\epsilon(E_\gamma)$, and the angular distribution $W_{\Pi L}(\theta,\phi)$:

$$I_S = \frac{A}{N_T \cdot N_\gamma(E_x) \cdot \epsilon(E_\gamma) \cdot W_{\Pi L}(\theta,\phi)}. \tag{1}$$

The scattering angle θ is defined as the angle between the incoming and the outgoing photons. The angle between the polarization plane, spanned by the direction of the electric field of the incoming photons and its direction of movement, and the direction of movement of the outgoing γ rays is denoted as ϕ. If an unpolarized photon source is utilized for the excitation, the angular distribution $W(\theta)$ is independent of ϕ. Since the angular distribution is dependent on the multipole order L and the radiation character Π, i.e. electric (E) or magnetic (M), the observed transition has to be characterized first. To assign the multipolarity L, the ratio ω of the angular distributions at two different scattering angles has to be calculated according to

$$\omega = \frac{W(90°)}{W(127°)} = \frac{A(90°)}{A(127°)} \cdot \frac{\epsilon(E_\gamma, 127°) \cdot \tau(127°)}{\epsilon(E_\gamma, 90°) \cdot \tau(90°)}. \tag{2}$$

For this purpose, $\theta = 90°$ and $\theta = 127°$ are best suited since the difference between the ratios for pure dipole, $\omega(L = 1) = 0.73$, and quadrupole transitions, $\omega(L = 2) = 2.28$, is the largest. The theoretical ratios are compared to the number of recorded events at the different scattering angles corrected for the corresponding detection efficiencies $\epsilon(E_\gamma,\theta)$ and the effective measuring times τ (see Eq. (2)).
For the determination of the radiation character Π, among others, a linearly-polarized γ-ray beam in the entrance channel can be used via the so-called analyzing power Σ_{hv}. This is defined by the angular distributions $W(\theta,\phi)$ ([29]):

$$\Sigma_{hv} = \frac{W(90°,0°) - W(90°,90°)}{W(90°,0°) + W(90°,90°)} = q \cdot \epsilon_{hv}. \tag{3}$$

The factor q corrects for the finite opening angles of the detectors and the degree of polarization. The quantity ϵ_{hv} denotes the experimental observable, i.e., the so-called asymmetry between the horizontal and the vertical detectors with respect to the polarization plane. It is calculated by replacing the theoretical angular distributions $W(\theta,\phi)$ by the number of recorded counts at the corresponding angles (θ,ϕ), corrected for $\epsilon(E_\gamma,\theta)$ and τ according to Eq. (2). The theoretically expected angular distributions of an electric (magnetic) dipole transition equal $W(90°,0°) = 0\,(1.5)$ for a detector in the polarization plane, and $W(90°,90°) = 1.5\,(0)$ for a detector positioned perpendicular to this plane. Therefore, the analyzing power is $\Sigma_{hv} = +1$ for an $M1$ transition and $\Sigma_{hv} = -1$ for an $E1$ transition. In the following, the detector in the polarization plane is denoted as the $M1$ detector and the detector perpendicular to the polarization plane as the $E1$ detector, due to the angular distributions.
The total decay width Γ equals the sum of all partial decay widths Γ_f, with f being the populated state, including the ground-state decay width Γ_0. When the ratio Γ/Γ_0, which is the inverse ground-state decay branching ratio, is known, the reduced transition strengths $B(\Pi L)\downarrow$ for the deexcitation process can be deduced via

$$\begin{aligned} B(E1)\downarrow\,[\mathrm{e^2fm^2}] &= 8.29 \cdot 10^{-4} \cdot \frac{\Gamma}{\Gamma_0}\,\frac{I_S[\mathrm{keVfm^2}]}{E_\gamma[\mathrm{MeV}]} \\ B(M1)\downarrow\,[\mu_\mathrm{N}^2] &= 7.46 \cdot 10^{-2} \cdot \frac{\Gamma}{\Gamma_0}\,\frac{I_S[\mathrm{keVfm^2}]}{E_\gamma[\mathrm{MeV}]}, \end{aligned} \tag{4}$$

where it was assumed that $E_\gamma = E_x$. To calculate the reduced transition strength for the excitation process, Eq. (5) holds.

$$B(\Pi L)\uparrow = \frac{2J+1}{2J_0+1} B(\Pi L)\downarrow. \tag{5}$$

Here, J and J_0 are the spin quantum numbers of the excited and the ground state, respectively.

II.2. Average quantities

Besides the investigation of individual transitions, average quantities can be determined by using, e.g., NRF experiments with a quasimonoenergetic γ-ray beam.
In this way, elastic decays, which are too weak to appear as distinct peaks in the deexcitation spectra, can be included. For this purpose, the total number of recorded NRF events $A(\mathrm{tot})$ in the excitation-energy region δE is investigated and corrected for the number of incoming photons in the same energy range $N_{\gamma,\mathrm{tot}}$. The elastic cross section $\sigma_{\gamma\gamma}$ can be calculated using [30, 31]

$$\sigma_{\gamma\gamma} = \frac{\sum_x I_{S,x\to 0}}{\delta E} \approx \frac{A(\mathrm{tot})}{N_T \cdot N_{\gamma,\mathrm{tot}} \cdot \overline{\epsilon(E_\gamma)}) \cdot W_{\Pi L}(\theta,\phi)}. \tag{6}$$

Here, $\overline{\epsilon(E_\gamma)})$ is the average detection efficiency. The expression in Eq. (6) is exact if the energy distribution of the photon beam is constant within the energy interval δE or the strengths of the individual transitions are equally distributed.
The observation of every inelastic transition for each individual state is experimentally challenging. Therefore, the average inelastic cross section $\sigma_{\gamma\gamma'}$ was defined for estimating the contribution of the inelastic-decay channel. The analysis assumes that most of the intermediate states k decay via the low-lying excited 2^+ states. If these 2^+ levels are not directly excited by the quasimonoenergetic photons, the number of recorded ground-state decays of these states $A(2^+)$ can be used to compute the average inelastic cross section $\sigma_{\gamma\gamma'}$ via [6]

$$\sigma_{\gamma\gamma'} = \frac{\sum_x I_{S,x\to k}}{\delta E} \approx \frac{A(2^+)}{N_T \cdot N_{\gamma,\mathrm{tot}} \cdot \epsilon(E_{2^+}) \cdot \overline{W_{\Pi L}(\theta,\phi)}}. \tag{7}$$

For this purpose, the integration of the photon flux has to be performed over the total excitation-energy region. The calculation of the angular distribution $\overline{W_{\Pi L}(\theta,\phi)}$ is challenging. Therefore, it is often assumed to be isotropic, because the lowest-lying states are fed by higher-lying ones and the angular distributions are driven towards isotropy.
The total, average photoabsorption cross section, which is the sum of the elastic and the inelastic cross sections $\sigma_\gamma = \sigma_{\gamma\gamma} + \sigma_{\gamma\gamma'}$, includes the complete dipole response, except for a small fraction of inelastic transitions bypassing the low-lying excited 2^+ states.

III. EXPERIMENTAL DETAILS

In order to study the photoresponse of ^{64}Ni, two complementary real-photon scattering experiments were performed. First, an energetically-continuous and mainly unpolarized bremsstrahlung beam, and second, a quasimonoenergetic and fully linearly-polarized photon beam generated by Laser-Compton Backscattering (LCB) were used as photon sources. The combination of both (γ,γ') experiments enables the differentiation between $E1$, $M1$, and $E2$ transitions and the extraction of quantities such as absolute, energy-integrated cross sections I_S (see Ref. [28] and references therein). In the following, experimental details of both complementary experiments are provided.

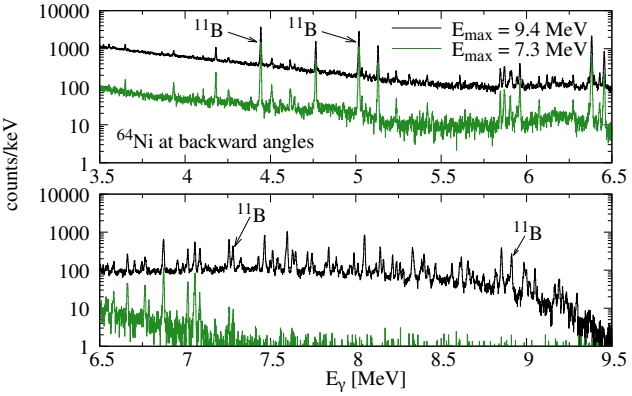

FIG. 1. Deexcitation spectra recorded by the detectors at backward angles of the 7.3 MeV (green) and the 9.4 MeV (black) bremsstrahlung measurements. The most prominent transitions of the calibration target ^{11}B are indicated.

Two bremsstrahlung measurements on ^{64}Ni were conducted at the γELBE facility at the Helmholtz-Zentrum Dresden-Rossendorf (HZDR) [32] using maximal photon energies of $E_{max} = 7.3$ MeV for 120 hours (LE measurement) and of $E_{max} = 9.4$ MeV for 80 hours (HE measurement). For the production of the bremsstrahlung beam with lower (higher) maximal photon energy, an electron beam with $E_{e^-} = 7.3$ MeV ($E_{e^-} = 9.4$ MeV) impinged on a 7 μm (12.5 μm) niobium radiator. The energetically-continuous bremsstrahlung beam was collimated (diameter of 4 cm at the target position) and impinged on the ^{64}Ni target disc with a diameter of 1.9 cm. It weighed 1456.56 mg and had an isotopic enrichment of 92.1 %. In addition to the target of interest, a ^{11}B target with a similar diameter and a weight of 300 mg (isotopic enrichment 99.5 %) served as calibration for the absolute photon-flux determination. The emitted γ rays were detected by four HPGe detectors, two at a scattering angle of $\theta = 90°$ and two at $\theta = 127°$ relative to the incoming photon beam. These were surrounded by lead shields for passive, and by Compton-suppression BGO shields for additional active background suppression. The distances between the detectors and the targets were 28 cm for the 90° and 32 cm for the backward (127°) detectors, respectively. By taking into account the corresponding opening angles of the detectors, the ratios of the angular distributions (cf. Eq. (2)) equal $\omega = 0.74$ and $\omega = 2.15$ for dipole and quadrupole transitions, respectively [19]. Figure 1 illustrates the summed deexcitation spectra of both detectors under backward angles for the low-energy (LE) measurement in green and the high-energy (HE) one in black. The neutron-separation energy of ^{64}Ni is $S_n = 9.7$ MeV.
A complementary $(\vec{\gamma},\gamma')$ experiment was performed on ^{64}Ni at the High Intensity γ-ray Source (HIγS) located

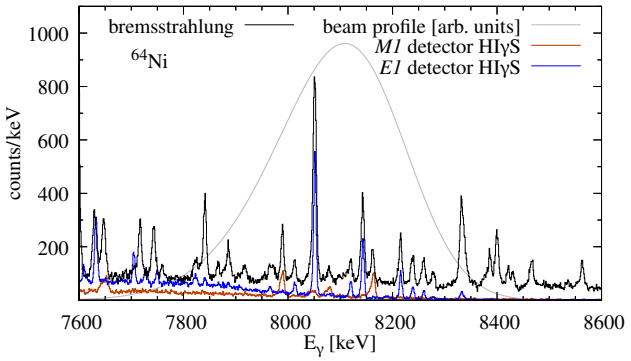

FIG. 2. The deexcitation spectra recorded by the $M1$ detector $(90°, 0°)$ and the $E1$ detector $(90°, 90°)$ at HIγS at a beam energy of 8.05 MeV are shown as orange and blue histograms, respectively. The photon-flux distribution in arbitrary units, which impinged on the target, is depicted in gray. The summed deexcitation spectrum recorded by the $\theta = 127°$ detectors of the bremsstrahlung experiment is illustrated in black.

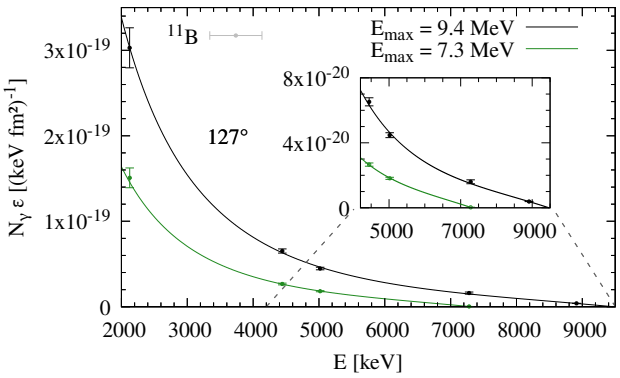

FIG. 3. The products of photon flux and detection efficiency of the backward detectors for the HE and the LE bremsstrahlung measurements are depicted in black and green, respectively. The shapes were scaled to the corresponding ^{11}B values (full circles). See text for details.

at TUNL utilizing a linearly-polarized and quasimonoenergetic γ-ray beam [33]. The photon beam passed a collimator with diameter of 1.9 cm before it impinged on the target. Because of the beam divergence, the beam had a diameter of approximately 2 cm at the target position. For the detection of the deexciting γ rays, the γ^3 setup was used [34]. It consisted of four HPGe detectors placed at $(\theta, \phi) = (90°, 90°)$, $(95°, 180°)$, $(135°, 45°)$, and $(135°, 315°)$. Although two HPGe detectors were positioned at backward angles in the experiment, only one of these was taken into account during the analysis due to uncertainties concerning the precise positioning of the other with respect to the target. Additionally, the γ^3 setup includes four $LaBr_3$ detectors which can be used for $\gamma - \gamma$ coincidence measurements. For this work, only the HPGe detectors were used.

In total, the experiment was performed with 26 different beam-energy settings between 4.33 MeV and 10 MeV (4.33, 4.48, 4.63, 4.75, 4.93, 5.13, 5.43, 5.63, 5.86, 6.15, 6.38, 6.55, 6.75, 6.95, 7.15, 7.35, 7.55, 7.8, 8.05, 8.3, 8.55, 8.8, 9.05, 9.3, 9.6, and 10.0 MeV) for approximately 3 to 4 hours each. The deexcitation spectra recorded by the $M1$ $(90°, 0°)$ and $E1$ $(90°, 90°)$ detectors at a beam energy of 8.05 MeV are displayed as orange and blue histograms, respectively, in Fig. 2. The excitation region is indicated by the beam profile (gray) in arbitrary units. In addition, the bremsstrahlung spectrum (black) recorded by the backward detectors is illustrated for comparison. For all measurements up to 9.05 MeV, the same ^{64}Ni target was used as for the bremsstrahlung experiment. For the three settings with the highest energies (9.3, 9.6, and 10 MeV), it was replaced by a ^{64}Ni target with a diameter of 8 mm and a total weight of 4 g (isotopic enrichment of 92.3 %). Before each measurement, a HPGe detector with a relative detection efficiency of 123 %, denoted as 0° detector, was positioned in the beam with reduced intensity for measuring the incoming photon-flux distribution.

IV. ANALYSIS AND RESULTS

In this section, the analysis procedures for obtaining the quantities introduced in Sec. II are discussed, and the results are presented.

For the determination of the full-energy-peak efficiencies $\epsilon(E_\gamma)$, source measurements up to 3.5 MeV were performed, and GEANT4 simulations [35–37] were used for the extrapolation to 10 MeV [38, 39].

For the bremsstrahlung measurement, the photon-flux distribution was determined by calculating the bremsstrahlung cross section [40] using the process description by Roche *et al.* [41], corrected by the screening of the nuclear Coulomb potential by the surrounding electrons [42]. Afterwards, the products of photon flux and efficiency $N_\gamma(E_x) \cdot \epsilon(E_\gamma)$ of the HE (black) and LE (green) measurements were individually scaled to known transitions of the calibration standard ^{11}B [43, 44].These are illustrated by filled circles in Fig. 3 for the detectors positioned at $\theta = 127°$.

For assigning multipolarities to the observed transitions, the intensity ratios were calculated according to Eq. (2). If the experimental intensity ratio is, within its 2σ range, in agreement with only one of the theoretical ratios of the angular distributions ($\omega = 0.74$ for a dipole and $\omega = 2.15$ for a quadrupole transition), a firm assignment was made. A tentative identification was proposed, if the experimental ratio is in accordance with only one of the theoretical values within its 3σ range. By assuming that only elastic transitions were observed, spin quantum numbers were associated to corresponding states due to the 0^+ ground state of ^{64}Ni (see Table I). Up to a γ-ray energy of 6.5 MeV, the low-energy measurement was used for multipolarity assignments and, for higher

energies, the 9.4 MeV one was preferred to minimize the effect of feeding contributions from higher-lying states to the levels of interest. Tentatively assigned spin quantum numbers are given in parentheses in Table I.

Afterwards, the energy-integrated cross sections I_S were computed using Eq. (1). For all firmly and tentatively identified dipole transitions, the energy-integrated cross sections I_S were calculated using the 127° detectors as the corresponding statistical uncertainties are smaller compared to those of the 90° detectors.

By using the HIγS data and applying Eq. (3), the radiation character was deduced. The index h (v) indicates that the detector positioned parallel (perpendicular) to the polarization plane, i.e., $\phi = 0°$ ($\phi = 90°$), was utilized. A firm (tentative) assignment was made if the asymmetries ϵ_{hv} are in agreement with only one of the simulated asymmetries within their 2σ (3σ) ranges, which include the finite opening angles of the detectors. For example, the simulation yielded values of $\epsilon_{hv} = -0.92$ for $E1$ and $\epsilon_{hv} = 0.90$ for $M1$ transitions with the setup configuration used for the beam energies between 5.86 MeV and 9.05 MeV. An additional uncertainty of 10 % was assumed for the simulated asymmetries to take into account a possible deviation of the absolute position of source and target. This uncertainty was justified by the observation of a discrepancy between the $E1$ and $M1$ detector (in total 10 %), when calculating the absolute photon flux. In the case of a tentative identification, the corresponding quantum number is given in parentheses in Table I.

In instances, where the multipolarity is not firmly known from the γELBE measurements and the asymmetry ϵ_{hv} agrees with the simulated one for an $E1$ transition, a multipole order of $L = 1$ was assumed. Indeed, the asymmetries of an $E1$ and an $M2$ transition are similar, but the probability to induce $M2$ transitions is negligible. Because the asymmetries ϵ_{hv} of $M1$ and $E2$ transitions are very similar as well, a complete characterization of the transition was done using the HIγS data in the case of an asymmetry value indicating an $M1$ transition. For this purpose, the backward ($\theta = 135°$) detector (indicated by the index b) of the γ^3 setup was taken into account and the asymmetries ϵ_{hb} and ϵ_{vb} were calculated analogously to Eq. (3) [45]. For a firm (tentative) assignment, the experimental values have to be in agreement within 2σ (3σ) with both simulated asymmetries ϵ_{hb} and ϵ_{vb}. These have uncertainties of 10 % as well.

At HIγS, a HPGe detector was used to record the shape of the incoming photon flux as stated in Sec. III. The resulting spectra consist of background radiation, γ rays directly stemming from the photon beam, and the resulting detector response. For the deconvolution of the latter two contributions, the unfolding code *Horst* was utilized [46]. It includes a Monte-Carlo approach for estimating the impact of uncertainties resulting from the fitting procedure and statistical uncertainties in the spectra as well as from the detector response (for details, see Ref. [46]). The detector response was obtained by performing GEANT4 simulations using the toolkit *utr* [39]. Figure 4 shows the result of the procedure for a beam energy of $E_{\mathrm{beam}} = 8.55$ MeV. The recorded and one of the unfolded spectra are illustrated as gray and black histograms, respectively. In addition, the photon distribution was calculated by using the parameters of the accelerator (red points) [47, 48]. A good agreement of both distributions is observed. Experimental values for the photon-current densities were determined using known ^{64}Ni transitions, analyzed in the bremsstrahlung measurement, by rearranging Eq. (1), and adding a correction for the different effective recording times of the individual detectors. For this purpose, the transitions detected by the HPGe detector at $\theta, \phi = 135°, 45°$ were used (light-blue points). Moreover, the dark blue and orange data points were deduced from the detector perpendicular to the polarization plane ($E1$ detector), and the detector parallel to the polarization plane ($M1$ detector), respectively. These were not utilized for the scaling of the photon-flux distribution.

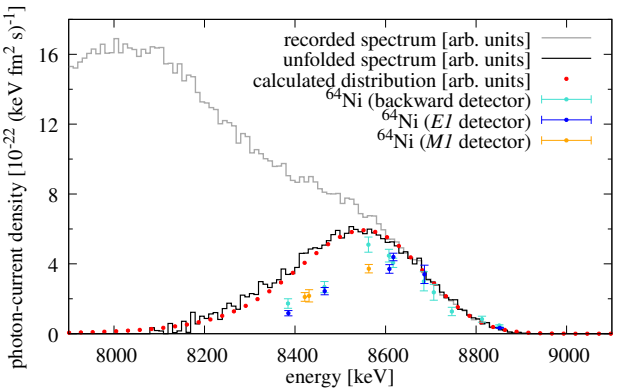

FIG. 4. The recorded photon spectrum of the 0° detector for a beam energy of 8.55 MeV is illustrated in gray and the deconvoluted spectrum as black histogram. In addition, the same quantity was calculated by utilizing the electron-beam parameters (red points). Experimentally expected photon-current densities using transitions of ^{64}Ni investigated with the backward, $E1$, and $M1$ detectors are displayed as light blue, dark blue, and orange circles, respectively.

In this experiment, a considerable deviation between the photon-flux distributions impinging on the 0° detector and on the ^{64}Ni target was observed. One possible explanation can be found in a non-optimal alignment of the target and the beam. Since the diameters of the target and the beam are very similar and the photon beam has a spatial energy-distribution (high energies are in the center of the beam and low energies at the edges), a displacement would lead to less lower-energy photons impinging on the target than on the 0° detector. Because of this, it was assumed that the number of photons of the recorded profile, which have energies higher than the centroid energy of the deconvoluted spectrum, is the same as the one incident on the ^{64}Ni target. Therefore, the high-energy sides of the deconvoluted 0° spectra

were used to describe the high-energy sides of the photon-flux distributions incident on the ^{64}Ni target. For determining the low-energy part, six beam-energy settings, for which the complete shapes of the photon fluxes impinging on the target are well described by the ^{64}Ni data points (indicated by arrows in Fig. 5), were used to define energy dependencies of the widths and centroid energies of the distributions. These were applied to deduce the energy distributions of photons for all beam-energy settings. This step was carried out for all Monte-Carlo results obtained from the deconvolution performed with the code *Horst*.

It has to be emphasized that this procedure is based on the assumption that all beam energies were affected in the same way by the possible displacement of the target. However, because the target was moved between the 5.63 MeV and 5.86 MeV measurements, and a ^{64}Ni target with a smaller diameter was used for beam energies above 9.05 MeV (for which the aforementioned effect would be even higher), this procedure was only used for all experimental runs between 5.86 MeV and 9.05 MeV. For beam energies below 5.86 MeV and above 9.05 MeV, an insufficient number of transitions of ^{64}Ni was observed in the bremsstrahlung experiment for determining the distributions applying the same procedure as explained above. Therefore, only relative quantities could be extracted for these beam energies.

After the determination of the photon-flux distributions, these were scaled to the ^{64}Ni values extracted for isolated transitions. For this procedure, two approaches are possible: (i) the scaling parameters are calculated for each beam energy individually, (ii) a more global method introduced in Ref. [49] is used. The result of the independent scaling is shown by the dashed curves in Fig. 5. For some beam-energy settings, only very few data points are available which introduces large uncertainties. Therefore, the global procedure presented in Ref. [49] was applied in addition. Here, advantage was taken of the fact that the low-energy background generated by atomic processes in the target is proportional to the total number of incident photons on the target per beam energy. Hence, the low-energy backgrounds for each detector and each beam energy were simulated. By integrating the simulated and experimental spectra in the same energy region (in this case between 370 keV and 480 keV) and calculating the ratios, the total numbers of photons impinging on the target during the measurement were determined. In this way and by using the same number of simulated photons for all beam energies, the photon-flux distributions were scaled relative to each other. At these low energies, the full-energy-peak efficiencies of the detectors at $\theta = 90°$ were significantly influenced by the absorption of photons within the target before reaching the detector which is dependent on the target's position. To minimize this effect, only the deexcitation spectra of the backward detector were utilized for this purpose. Then, all relatively-scaled photon distributions were simultaneously scaled to all ^{64}Ni values. A more detailed description of this method can be found in Ref. [49].

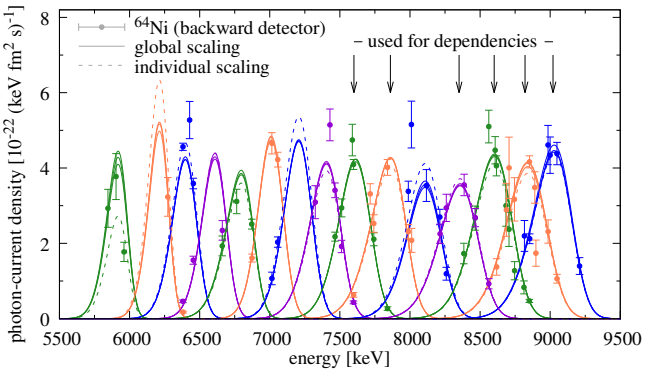

FIG. 5. The absolute photon-current densities are shown for all beam energies between 5.86 MeV and 9.05 MeV. The absolute photon-current densities were obtained by scaling, on the one hand, each distribution to the corresponding ^{64}Ni data (dashed curve) and, on the other hand, all shapes to the ^{64}Ni data of all beam-energy settings at once. The different colors serve for the distinction between the different beam-energy settings. See text for further details.

As can be seen in Fig. 5, the dashed and solid curves are in good agreement for beam energies with data points distributed over the total beam-energy profile. In these cases, the individual scaling should also provide reliable values with small uncertainties.

The energy-integrated cross sections I_S of transitions only observed in the HIγS experiment or which were possibly affected by feeding or single-escape contributions in the bremsstrahlung experiment, were calculated using the HIγS data and are identified as such in Table I. For the computation of I_S for an $E1$ ($M1$) transition, the detector perpendicular (parallel) to the polarization plane was used. Because the absolute photon-current densities were determined using the backward detector, correction factors had to be applied for the calculation of absolute quantities using the $E1$ and $M1$ detectors. These correction factors take into account uncertainties associated with inaccuracies of the relative products of detection efficiency and angular distribution with respect to the backward detector. The absolute photon-current densities determined using the backward detector were scaled to transitions investigated with the corresponding $\theta = 90°$ detector. For both detectors, the deviations were approximately 5 %. Only $E1$ ($M1$) transitions were utilized for the scaling of the photon-current densities of the detector perpendicular (parallel) to the polarization plane, therefore, no correction factor could be determined for the other radiation character, and it was assumed to be negligible.

For the estimate of the uncertainty, a Monte-Carlo approach has been used. Each experimental quantity going into the calculations of the energy-integrated cross sections according to Eq. (1), such as the peak area A of the corresponding transition or the values entering the

photon-flux determination, was varied within its statistical uncertainty for each iteration. The mean I_S and its standard deviation were determined from the resulting probability distributions for the outcomes of the two flux-scaling procedures separately. Subsequently, the Monte-Carlo approach was once again applied to average both results, yielding the final energy-integrated cross section. The corresponding standard deviation represents the statistical uncertainty. The systematic uncertainty associated with the difference between the two scaling approaches was extracted from the discrepancies between the final I_S values and the values obtained from the two separate procedures. Furthermore, a systematic uncertainty of 10 % was applied, reflecting the determination of the product of efficiency and photon flux at γELBE. This uncertainty accounts for the accuracy of the fit functions used to describe the ^{11}B calibration points. Both contributions were combined and are presented in Table I as systematic uncertainties. When extracting the energy-integrated cross sections and reduced transition strengths from the γELBE measurement, only the latter is quoted as systematic uncertainty. To minimize the statistical uncertainties, the peak area extracted from the detector perpendicular (parallel) to the polarization plane was used for an identified $E1$ ($M1$) transition. If a radiation-character assignment was not possible and the HIγS results had to be used, the energy-integrated cross sections for both possibilities are given. Then, the first value was extracted from the perpendicular $\phi = 90°$ detector assuming an $E1$ transition and the second from the parallel $\phi = 0°$ detector assuming an $M1$ transition. For known $E2$ transitions, it was observed that feeding contributions occur also in the LE bremsstrahlung measurement up to approximately 4.5 MeV and the HIγS data only cover the energy range above 4.3 MeV. Therefore, only ground-state transitions above this energy are included in Table I. It should be pointed out that below 5.86 MeV no absolute photon-current densities could be determined for the HIγS data. Hence, energy-integrated cross sections and transition strengths may be contaminated by feeding and single-escape contributions below this energy.

TABLE I: The table provides excitation energies E_x and assigned spin and parity quantum numbers J^π. Tentatively assigned ones are given in parentheses. The energy-integrated cross section I_S and the corresponding product of reduced transition strength $B(\Pi L)\downarrow$ and Γ_0/Γ are listed. When the radiation character could not be determined, the reduced transition strengths for both possibilities are given. The statistical and systematic uncertainties are quoted in the first and second parentheses, respectively. If the parity quantum number was assigned by comparing the energy-integrated cross sections, it is indicated with an asterisk. Two I_S values are given if they were extracted from the HIγS data and the radiation character is unknown. The first (second) value corresponds to an assumed $E1$ ($M1$) transition deduced from the spectra of the $E1$ ($M1$) detector. A systematic uncertainty of ± 1 keV is assumed for the excitation energies.

E_x [keV]	J^π	I_S [keV fm^2]	$B(E1)\downarrow \cdot \Gamma_0/\Gamma$ [10^{-5}e^{2}fm^2]	$B(M1)\downarrow \cdot \Gamma_0/\Gamma$ [$10^{-3}\mu_N^2$]
4617	1^+	1.55(9)(16)		25.1(14)(25)
4765	1^-	11.79(22)(118)	205(4)(20)	
4995[a]	1^+			
5059	1	0.51(7)(5)	8.4(12)(8)	7.5(11)(8)
5130	1^-	11.81(24)(118)	190(4)(19)	
5419	1	0.80(9)(8)	12.1(14)(12)	10.9(12)(11)
5640	$1^{(+)}$	0.38(7)(4)		5.0(10)(5)
5846	1^-	2.90(17)(29)	41.0(24)(41)	
5905	1^-	2.56(17)(26)	35.8(24)(36)	
5961	1^-	6.06(25)(61)	84(3)(8)	
6074	1^-	4.3(12)(7)[b]	58(16)(9)	
6166	1^+	1.25(17)(13)		15.1(20)(15)
6273	1^+	2.16(14)(22)		25.6(17)(26)
6382	1^-	48.5(4)(49)	629(6)(63)	
6402[a]	1^+	0.68(5)(10)[b]		7.9(6)(11)
6429	1^+	2.88(15)(29)		33.3(18)(33)
6455	1^-	17.98(28)(180)	230(4)(23)	
6537	1^+	0.83(12)(8)		9.5(14)(9)
6582	1^-	1.70(14)(17)	21.4(18)(21)	
6663	1^-	5.16(20)(52)	64.0(25)(64)	
6687[a]	$1^+, 2^+$	0.57(7)(6)[b]		6.4(8)(6)
6765	1^-*	4.75(20)(48)	58.1(25)(58)	
6875	1^-	19.3(3)(19)	232(4)(23)	
7016	1^-	8.25(25)(83)	97.3(30)(97)	
7050	1	0.44(7)(6)[b]	5.2(9)(7)	
		0.23(5)(3)[b]		2.5(5)(3)
7058	1^-	15.2(3)(15)	178(4)(18)	
7086	1^-	5.3(3)(11)[b]	62(4)(13)	
7175	1^-	1.12(18)(11)	12.9(21)(13)	
7258	1^-	18.0(8)(36)[b]	205(9)(42)	
7272	1^+	0.76(7)(15)[b]		7.8(7)(16)
7328	1^-	4.4(3)(4)	50(4)(5)	
7387[a]	1, 2	0.53(14)(7)[b]	6.0(16)(8)	
		0.67(7)(8)[b]		6.7(7)(8)

Table I - *Continued.*

E_x [keV]	J^π	I_S [keV fm^2]	$B(E1)\downarrow\cdot\Gamma_0/\Gamma$ [10^{-5}e^{2}fm^2]	$B(M1)\downarrow\cdot\Gamma_0/\Gamma$ [$10^{-3}\mu_N^2$]
7430	1^-	5.71(27)(57)	64(3)(6)	
7457	1	2.18(30)(22)	24.1(34)(24)	21.7(30)(22)
7466	1^-	31.1(5)(31)	344(6)(34)	
7499	1^-	3.83(21)(47)[b]	42.2(23)(52)	
7513	1^-	11.1(3)(11)	122(4)(12)	
7557	1^-	2.60(24)(26)	28.5(26)(28)	
7590	1^-	7.8(4)(8)	85(4)(8)	
7599	1^-	42.1(6)(42)	459(7)(46)	
7631	1^-	10.3(3)(11)[b]	112(3)(12)	
7648	1^-	10.1(3)(11)[b]	109(3)(12)	
7687[a]	1, 2	1.91(18)(21)[b]	20.6(19)(22)	
		0.78(9)(9)[b]		7.6(8)(8)
7717	1^+*	11.5(4)(11)		111(4)(11)
7743	1^-	11.5(4)(12)	123(4)(12)	
7760	1^+	2.50(26)(25)		24.0(25)(24)
7824	1^-	1.92(17)(24)[b]	20.3(18)(25)	
7841	1^-	17.4(4)(17)	183(5)(18)	
7866	1^-	3.54(30)(35)	37(3)(4)	
7878	1	0.89(13)(11)[b]	9.3(14)(11)	
		1.12(12)(13)[b]		10.6(11)(12)
7887	1^-	6.37(25)(77)[b]	66.8(26)(81)	
7907	1^-	1.24(27)(12)	13.0(28)(13)	
7918	1	0.77(12)(9)[b]	8.1(12)(10)	
		1.60(13)(19)[b]		15.1(12)(18)
7966	1^-	3.5(4)(3)	36(4)(4)	
7990	1^+	11.2(4)(11)		105(4)(10)
8013	1^-	4.4(3)(4)	46(3)(5)	
8043	1	3.6(6)(7)[b]	37(6)(7)	
		1.59(18)(27)[b]		14.7(17)(25)
8052	1^-	47.1(11)(78)[b]	484(11)(80)	
8079	1^+	2.67(29)(27)		24.6(27)(25)
8120	1^-	5.2(3)(5)	53(4)(5)	
8144	1^-	20.0(5)(33)[b]	203(5)(34)	
8163	1^+	8.4(4)(8)		77(4)(8)
8216	1^-	12.4(4)(12)	124(4)(12)	
8239	1^-	8.4(5)(11)[b]	84(5)(12)	
8260	1^-	7.9(4)(8)	79(4)(8)	
8278	1	4.2(3)(4)	42(3)(4)	37.7(29)(38)
8333	1^-	23.9(11)(32)[b]	238(10)(32)	
8342	1^-	12.5(10)(17)[b]	124(10)(17)	
8360[a]	1^+	0.62(12)(10)[b]		5.5(11)(9)
8376	1^+	3.6(4)(4)		32(4)(3)
8387	1^-	11.3(5)(11)	112(5)(11)	
8401	1^-	16.5(5)(22)[b]	163(5)(22)	
8421	1^+	6.0(5)(6)		53(4)(5)
8431	1^+	4.2(5)(4)		37(4)(4)
8467	1^-	10.6(5)(11)	104(5)(10)	

Table I - *Continued.*

E_x [keV]	J^π	I_S [keV fm^2]	$B(E1)\downarrow\cdot\Gamma_0/\Gamma$ [10^{-5}e^{2}fm^2]	$B(M1)\downarrow\cdot\Gamma_0/\Gamma$ [$10^{-3}\mu_N^2$]
8495[a]	1^-	2.09(31)(26)[b]	20.4(30)(25)	
8520[a]	1^-	0.89(22)(13)[b]	8.6(22)(13)	
8536	$1^{(-)}$	1.40(20)(17)[b]	13.6(20)(16)	
8564	1^+*	9.7(5)(10)		84(4)(8)
8586[a]	1^+	1.26(11)(16)[b]		10.9(10)(14)
8609	1^-	11.6(6)(12)	111(6)(11)	
8619	1^-	17.3(7)(17)	166(6)(17)	
8657	1^-	15.2(5)(18)[b]	145(5)(17)	
8666	1^-	6.10(30)(74)[b]	58.3(28)(70)	
8680	1^+	0.78(11)(9)[b]		6.7(9)(8)
8687	1^-	5.8(8)(6)	55(8)(5)	
8710	1^-	4.2(4)(4)	39(4)(4)	
8748	1^-	5.6(5)(6)	53(4)(5)	
8778[a]	1^-	1.08(25)(16)[b]	10.2(24)(15)	
8786[a]	(1^-)	1.27(25)(17)[b]	12.0(24)(16)	
8818	1^-	8.4(7)(8)	79(7)(8)	
8826	1^-	7.4(4)(9)[b]	69(3)(9)	
8844	1^-*	3.3(5)(3)	31(5)(3)	
8854	1^-	51.2(12)(51)	478(11)(48)	
8865	1	3.89(25)(50)[b]	36.3(24)(46)	
		1.28(13)(17)[b]		10.7(11)(42)
8883	1^-	4.4(5)(4)	41(5)(4)	
8893	1^-	8.5(6)(8)	79(6)(8)	
8903	1^-	6.8(6)(7)	63(6)(6)	
8913[a]	1^+	0.93(15)(12)[b]		7.8(13)(10)
8921[a]	1^-	2.26(24)(31)[b]	21.0(22)(29)	
8934[a]	1^-	1.60(20)(20)[b]	14.8(19)(19)	
8959	1	2.35(45)(24)	21.7(41)(22)	19.6(37)(20)
8986	1^-	23.4(22)(23)	216(20)(22)	
8993	$1^{(-)}$	8.9(19)(9)	82(18)(8)	
9000	1^-	17.3(13)(17)	159(12)(16)	
9009	1	2.52(72)(25)	23.2(66)(23)	20.8(59)(21)
9019	1^-	9.9(7)(10)	91(7)(9)	
9034[a]	1, 2	1.21(20)(15)[b]	11.1(19)(14)	
		1.04(13)(11)[b]		8.6(10)(9)
9050	1^-	19.1(9)(19)	175(8)(17)	
9064	1^-	2.84(54)(28)	25.9(49)(26)	
9076[a]	(1^+)	0.57(10)(6)[b]		4.6(8)(5)
9091[a]	(1^-)	1.78(17)(19)[b]	16.2(16)(18)	
9109[a]	1^+	1.07(13)(11)[b]		8.8(11)(9)
9123[a]	1^-	0.98(17)(11)[b]	8.9(15)(10)	
9132[a]	1, 2	1.13(18)(13)[b]	10.3(16)(12)	
		0.73(12)(8)[b]		6.0(10)(6)
9167	1^-	9.3(8)(9)[b]	84(7)(8)	
9180	1^+	2.55(64)(25)		20.7(52)(21)
9192	1^-	19.0(11)(19)	171(10)(17)	
9212	1^-	8.9(8)(9)	80(7)(8)	

Table I - *Continued.*

E_x [keV]	J^π	I_S [keV fm^2]	$B(E1)\downarrow\cdot\Gamma_0/\Gamma$ [10^{-5}e^{2}fm^2]	$B(M1)\downarrow\cdot\Gamma_0/\Gamma$ [$10^{-3}\mu_N^2$]
9234	1^-	8.8(8)(9)	79(7)(8)	
9265	$1^{(-)}$	3.0(6)(3)	27.1(56)(27)	
9295	1^-	9.8(9)(10)	87(8)(9)	
9331[a]	(1^-)			
9339[a]	1^-			
9348[a]	$1^+, 2^+$			
9356[a]	1^-			
9363[a]	1, 2			
9369	1^-	6.0(10)(6)	53(9)(5)	
9402[a]	1, 2			
9411[a]	1^-			
9426[a]	1, 2			
9463[a]	1^-			
9474[a]	1^-			
9490[a]	1^-			
9502[a]	1, 2			
9513[a]	1^-			
9522[a]	1^-			
9539[a]	$1^+, 2^+$			
9548[a]	1, 2			
9558[a]	1^-			
9575[a]	1^-			
9600[a]	(1^-)			
9635[a]	(1^-)			
9641[a]	1, 2			
9651[a]	1, 2			

[a] only observed at HIγS
[b] determined from HIγS data

In four cases, the radiation character was assigned by comparing the two possible I_S values determined from the HIγS data to the γELBE result. The corresponding energy-integrated cross sections are presented in Table II. These spin-parity quantum numbers are indicated by an asterisk in Table I. Feeding contributions to these states, which would affect the energy-integrated cross sections extracted from the bremsstrahlung analysis, were excluded due to the comparison of the HE and LE measurements at γELBE.

In all, 87 1^- states and 23 1^+ states were firmly identified between 4.3 MeV and S_n by combining the HIγS and γELBE results. Eight states were tentatively identified as 1^- states and two as 1^+ ones. For eleven states, $J = 1$ was determined.

Besides the investigation of individual transitions, average elastic cross sections $\sigma_{\gamma\gamma}$ were determined for all beam-energy settings with known absolute photon-current densities from the HIγS data, i.e., for all beam energies between 5.86 and 9.05 MeV. For this purpose, the recorded deexcitation spectra were deconvoluted using the code *Horst*. Afterwards, the absolute photon-current density and the deconvoluted spectra were integrated in the same energy range δE to apply Eq. (6). Because of the non-constant photon-current density and individual, very strong transitions of ^{64}Ni, the width of the integration interval was chosen to be $\delta E = 50$ keV. No $E2$ transition was identified in the state-to-state analysis above 5 MeV. Hence, only the $E1$ and $M1$ channels of the elastic cross section were disentangled following the approach described in Ref. [45]. Because the recorded deexcitation spectra of both $\theta = 90°$ detectors consist of superpositions of $E1$ and $M1$ transitions, two linear equations with two unknown parameters, $\sigma_{\gamma\gamma}(M1)$ and $\sigma_{\gamma\gamma}(E1)$, were set up according to Eq. (6). As described above, the determination of the absolute photon-current densities using the $E1$ and $M1$ detectors showed 5 % discrepancies with respect to the backward detector. This corresponds to uncertainties of the product of angular distribution and efficiency. As stated above, these deviations were quantified for $E1$ ($M1$) transitions for the $E1$ ($M1$) detector, but no correction could be determined for the other radiation character. Therefore, it was only applied to the corresponding term in the individual linear equation. However, for the other radiation character, i.e., the $M1$ ($E1$) channel recorded by the detector perpendicular (parallel) to the polarization plane, no correction factor could be determined and applied.
The linear equations were solved for all combinations of photon flux and peak area extracted in the previous steps. For the determination of elastic cross sections and their corresponding statistical and systematic uncertainties, the same procedure used for the energy-integrated cross section was applied.
Because of some rest gas present in the beam line during the measurements at $E_{\mathrm{beam}} = 5.86$ MeV and $E_{\mathrm{beam}} = 6.15$ MeV, the deconvoluted deexcitation spectra contained, even after the deconvolution, events not resulting from NRF reactions in the target. Hence, these two energy runs were neglected in this part of the analysis.
In Panel (a) of Fig. 6, the $M1$ and the $E1$ average elastic

TABLE II. Energy-integrated cross sections determined from the bremsstrahlung (γELBE) and the HIγS experiments using the $E1$ and the $M1$ detectors are given for transitions with unknown radiation character due to the asymmetry ϵ_{hv}. In the first parenthesis, the statistical uncertainty, and in the second, the systematical uncertainty of the photon flux at HIγS are given. The uncertainty of the photon flux at γELBE is not included.

E_x [keV]	I_S [keV fm^2]		
	γELBE	HIγS $E1$ det.	HIγS $M1$ det.
6765	4.75(20)	4.32(19)(12)	1.06(8)(3)
7717	11.5(4)	3.16(31)(7)	10.73(36)(19)
8564	9.7(5)	3.37(25)(7)	8.71(26)(17)
8844	3.3(5)	3.43(31)(11)	1.86(15)(5)

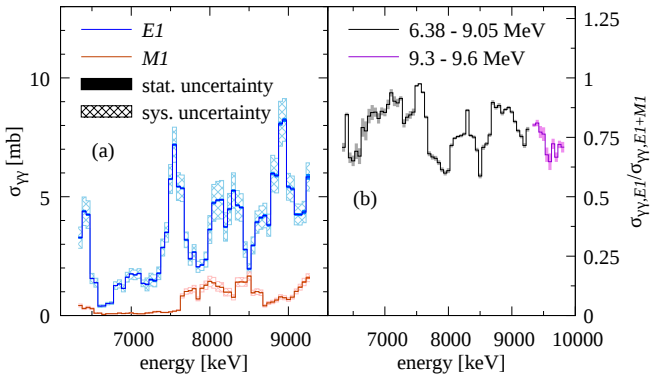

FIG. 6. In Panel (a), the moving average over a range of 200 keV of the elastic cross sections of the $E1$ and $M1$ channels deduced in 50 keV steps is shown in blue and orange, respectively. The statistical uncertainties (shaded areas) are small. The systematic uncertainties (resulting from the photon fluxes of the γELBE and HIγS measurements, see text) are depicted as crosshatched areas. Panel (b) illustrates the fraction of the $E1$ contribution with respect to the total cross section. This ratio was not only calculated for beam energies between 6.38 and 9.05 MeV (black), but also for the beam-energy settings of 9.3 and 9.6 MeV for which absolute measurements were not possible (purple).

cross sections in terms of moving averages over a range of 200 keV are displayed in orange and blue, respectively. Furthermore, the fraction of the $E1$ contribution normalized to the sum of $E1$ and $M1$ elastic cross sections is given in Panel (b) of Fig. 6. The calculation of this ratio has the advantage that systematic uncertainties are eliminated. Additionally, it could also be determined for the beam-energy settings of 9.3 and 9.6 MeV where the photon-current densities are unknown (purple data in Fig 6). The 10 MeV deexcitation spectra recorded by the HPGe detectors do not show any strength and, therefore, no results are given. It can be observed that the $M1$ channel is weak compared to the $E1$ channel for all energies, except between 7.5 and 8.5 MeV. In this energy region, the $M1$ channel contributes more to the average elastic cross section and the strengths of both channels are partly comparable. Above 8.5 MeV, the $M1$ contribution drops again. This is indicated in Panel (b) of Fig. 6 as well.

To determine the average inelastic cross section $\sigma_{\gamma\gamma'}$, the ground-state transitions of the 2^+_1 state at 1346 keV, the 2^+ levels at 3154 and 3275 keV, and of a state at 2972 keV, which spin-parity quantum number is given as $(1, 2^+)$, were investigated [50]. By applying Eq. (7), extracting the peak areas $A(2^+)$ of the ground-state decays of the low-lying 2^+ states from the deexcitation spectra of each HPGe detector individually, and assuming $\overline{W_{\Pi L}(\theta, \phi)} \approx 1$, the average inelastic cross sections $\sigma_{\gamma\gamma'}$ were calculated. The investigation using all HPGe detectors accounts for systematic uncertainties introduced by, e.g., detection efficiencies at low γ-ray energies or not completely-isotropic angular distributions. For the uncertainty estimate, the Monte-Carlo approach was used by combining each extracted photon-current density (as explained above) with the peak areas $A(2^+)$, which were varied within their statistical uncertainties following a Gaussian distribution. The determination of uncertainties was performed in analogy to the procedure described before for the elastic cross section. Additionally, the contribution from the extraction of the inelastic cross section using the different HPGe detectors was included.
The results serve only as estimate of the average inelastic cross sections since the non-constant photon distribution could not be taken into account. Therefore, the photon-current densities were integrated over the total excitation-energy region. The sum of the average inelastic cross sections corresponding to all observed ground-state decays of the low-lying 2^+ states are presented in dark green in Fig. 7.
In addition, Fig. 7 illustrates the comparison of the average elastic cross sections corresponding to the $E1$ channel, extracted in $\delta E = 50$ keV steps in terms of the moving average over a range of 200 keV (blue data), and from the investigation of the complete excitation-energy region at once $\delta E = E_{\mathrm{beam,total}}$ (black squares). The general trends of the average elastic cross sections $\sigma_{\gamma\gamma,E1}$ determined using both methods are in good agreement although the fine structure of the strength is, of course, better described by the continuous analysis in 50 keV steps. Because of this agreement, it was concluded that the average inelastic cross section can be estimated by using the determined $\sigma_{\gamma\gamma'}$ values: In Fig. 7, the sums of the average elastic $E1$ cross sections $\sigma_{\gamma\gamma,E1}$ and the average inelastic cross sections $\sigma_{\gamma\gamma'}$ are illustrated in brown, i.e., the total photoabsorption cross section $\sigma_{\gamma,E1}$ is displayed. Because $\sigma_{\gamma\gamma'}$ includes the $E1$ and $M1$ channels, the depicted photoabsorption cross sections $\sigma_{\gamma,E1}$ provide only an upper limit. Nevertheless, the importance of including the inelastic-decay channel at high excitation energies can be seen.

V. DISCUSSION

In this section, the experimental results are compared to theory. Here, the $E1$ response contained in elastic transitions is compared to calculations performed within the relativistic equation of motion (REOM) framework. This is part of the relativistic nuclear field theory (RNFT) that represents the most optimal balance of fundamentality, predictive power, and feasibility for nuclear structure calculations. The apparent advantages of RNFT are its covariance, connection to particle physics, non-perturbative character, and transparent treatment of sub-leading contributions to the nucleon-nucleon forces in complex nuclei. The only input to RNFT is the meson masses and coupling constants, slightly renormalized in the framework of the covariant density functional theory, compared to their vacuum values and universal across the nuclear chart. Up to now, the REOM has not been

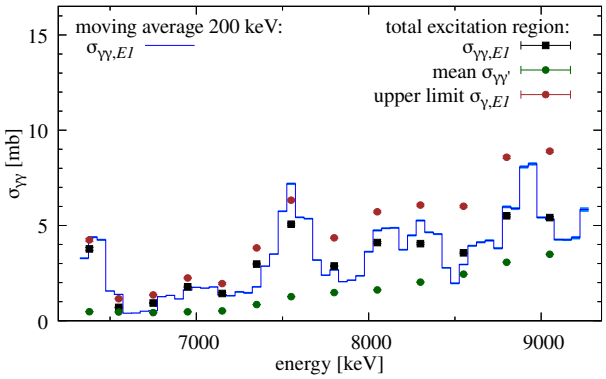

FIG. 7. The comparison of the average elastic cross section $\sigma_{\gamma\gamma,E1}$ with respect to the $E1$ channel, extracted in 50 keV steps in terms of the moving average over an energy range of 200 keV (blue histogram), and from the investigation of the total excitation-energy region at once (black points) is shown. Additionally, the average inelastic cross sections $\sigma_{\gamma\gamma'}$, which include $E1$ and $M1$ transitions, are illustrated in dark green. The corresponding upper limit for the photoabsorption cross section $\sigma_{\gamma,E1}$ was calculated (brown). Only statistical uncertainties are included. For details, see text.

adopted for calculations of nuclear response of unnatural parity in the neutral sector. Therefore, shell-model calculations were performed to interpret the $M1$ strength of individual transitions of ^{64}Ni observed in the experimental data. The shell-model approach is capable of providing accurate treatment of complex multiparticle-multihole configurations in sufficiently small model spaces, that is, the case of the $M1$ response. However, it is more difficult to extend to model spaces covering two major shells required for the $E1$ excitations in the energy interval under study.
The most important details concerning both calculations are given below.

V.1. Relativistic equation of motion approach

The most convenient tool to quantify the nuclear strength functions over a wide range of energies is response theory. In major textbooks and many practical applications, response theory is confined by the random phase approximation (RPA) or its superfluid variant, the quasiparticle RPA (QRPA). In the context of the most fundamental ab initio equation of motion (EOM) framework [51, 52], QRPA neglects completely the dynamical interaction kernel, while in the diagrammatic formulation, (Q)RPA is associated with a one-loop approximation. In Rowe's EOM [53], (Q)RPA is represented by the simplest one-particle-one-hole (two-quasiparticle) $1p1h$ (2q) excitation operator generating the excited states by its action on a non-correlated ground state, while more accurate solutions require higher-complexity ($npnh$) correlations in both the excited and ground states of the system.

(Q)RPA is known to reproduce some basic features of giant resonances and soft modes. However, a detailed and accurate description of nuclear spectra requires a much more advanced theory. All the approximations beyond (Q)RPA were shown to be derivable from the dynamical kernel of the ab initio EOM for the two-fermion response function [54, 55]. In particular, the leading approximation beyond (Q)RPA is the quasiparticle-vibration coupling (qPVC) in the minimal coupling scheme including $2q\otimes phonon$ configurations in the two-fermion in-medium propagator, where the phonon represents correlated $2q$ pairs. Realistic implementations of this approach may employ effective interactions, which yield quite reasonable phonons already within (Q)RPA, combined with subtraction restoring the self-consistency of the ab initio framework [56]. The minimal qPVC extension of (Q)RPA by the $2q \otimes phonon$ configurations is often insufficient, and higher configuration complexity may be needed to describe fine details of nuclear spectra. The two-fermionic cluster decomposition of the fully correlated dynamical kernel of the response function suggests that the next-level complexity non-perturbative approximation is the $2q\otimes 2phonon$ or correlated six-quasiparticle configurations in the intermediate propagators.

Based on the recent developments of Refs. [54, 55], calculations for the electromagnetic dipole response of ^{64}Ni were performed with the NL3* meson-exchange interaction [57]. This parametrization (an upgrade of NL3) demonstrates a reliable performance in the description of nuclear masses and radii [58]. Furthermore, the NL3* has the advantage of its ansatz being separable in the momentum representation, which allows for an economical and efficient implementation for calculations of the nuclear response.
The calculations were conducted in the three many-body approximations of growing complexity: relativistic QRPA (RQRPA), relativistic $2q \otimes phonon$ EOM (REOM^2) and relativistic $2q\otimes 2phonon$ EOM (REOM^3). The upper index in REOM^n is adopted as a universal complexity index, marking the maximal number of correlated or non-correlated particle-hole configurations in the intermediate propagators: $2p2h$ for REOM^2 and $3p3h$ for REOM^3. Natural-parity phonons up to 20 MeV with $J = [1, 6]$ were used in both REOM^2 and REOM^3, and the intermediate $2q\otimes phonon$ propagators with both parities and $J = [0, 6]$ were included in the model space of REOM^3. The $2q$ configurations were included up to 100 MeV, while the $2q \otimes phonon$ ones were accommodated up to 30 MeV. Including $2q\otimes 2phonon$ configurations up to high energy is technically challenging, and the energy cutoff of 25 MeV was the maximum that is feasible on the supercomputer cluster at Western Michigan University. Further details are similar to those of calculations presented in Ref. [59].

REOM^2, previously dubbed as relativistic (quasiparticle) time blocking approximation (R(Q)TBA), brings the major refinement and significant improvement of the description as compared to RQRPA, as displayed in Panels (a) and (b) of Fig. 8. However, it can be observed

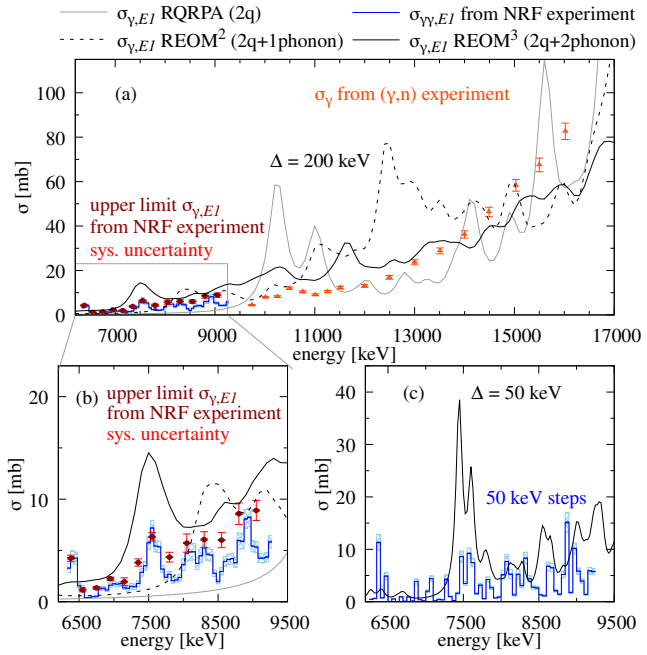

FIG. 8. Top: The $E1$ photoabsorption cross section $\sigma_{\gamma,E1}$ of ^{64}Ni in the three many-body approximations of growing complexity: relativistic QRPA (RQRPA) (gray), relativistic $2q \otimes phonon$ EOM (REOM^2) (dashed black), and relativistic $2q \otimes 2phonon$ EOM (REOM^3) (solid black). The results up to 17 MeV were obtained with the $\Delta = 200$ keV smearing parameter (the imaginary part of the energy argument and corresponding to half the width of the individual peaks) in comparison with the experimental NRF elastic cross section $\sigma_{\gamma\gamma,E1}$ (blue). These data are depicted as moving averages over a range of 200 keV. The statistical (systematic) uncertainties are shown as blue shaded (light-blue crosshatched) areas. Furthermore, the upper limits for the $E1$ photoabsorption cross sections $\sigma_{\gamma,E1}$, which also include the average inelastic cross sections, and the statistical uncertainties determined in the NRF experiment are depicted as dark-red points. The corresponding systematic uncertainties are illustrated as light-red error bars. Additionally, the total photoabsorption cross section σ_γ extracted from a (γ, n) measurement by Utsonomiya *et al.* (orange triangles) [60] are given. Panel (b): the same data as in (a) but just up to 9500 keV to emphasize the energy region associated with the PDR. Panel (c): for a better comparison of the fine structure observed in the NRF experiment with the REOM^3 calculation, the experimental results extracted in 50 keV steps are illustrated together with the REOM^3 results obtained with a smearing parameter of $\Delta = 50$ keV.

that more complex configurations than $2q \otimes phonon$ are needed for a more accurate description of the experimental data. By adding more complex $2q \otimes 2phonon$ configurations in REOM^3 the strength distribution is still visibly changed. It can be seen that a significant portion of the strength moves toward lower energies. In particular, the pygmy-resonance domain below 10 MeV manifests considerable structural differences between the REOM^2 and REOM^3 approaches (cf. Panel (b) of Fig. 8). On the theory side, the model-independent framework [54, 61] indicates that, in principle, configurations up to NpNh complexity have to be included to solve the many-body problem of N particles exactly. Therefore, any effort toward high-complexity configurations should improve the description of a many-body system. However, a comparison of the RQRPA, REOM^2, and REOM^3 numerical results indicates that the quantitative importance of complex configurations decreases with complexity. Hence, it can be assumed that reaching the desired accuracy is feasible within the model spaces of maximal complexity not significantly exceeding $2q \otimes 2phonon$ in the coupling regimes of nuclear structure.

The theoretical results given in Fig. 8 represent the total $E1$ photoabsorption cross sections $\sigma_{\gamma,E1}$. The average $E1$ elastic cross sections $\sigma_{\gamma\gamma,E1}$ deduced from the NRF measurements are displayed in blue. The experimental upper limits of the $E1$ photoabsorption cross section shown in dark red include the inelastic decay channel for which no distinction between $E1$ and $M1$ transitions was possible, as described in the previous section. Hence, these results represent upper limits with respect to the $E1$ channel. In the case of the photoabsorption cross section deduced from the (γ, n) experiment (orange), also the $M1$ channel is included, but it was theoretically shown in Ref. [60] that this contribution is negligible above approximately 10.5 MeV. Because no absolute cross sections could be determined between 9.3 MeV and S_n in this NRF measurement, a conclusive comparison of the NRF and the (γ, n) data is not possible. However, there are indications of additional $E1$ strength and structures on top of the low-energy tail of the IVGDR in the PDR region.

Whereas the RQRPA and the REOM^2 results do not show strength distributions comparable to the NRF data, the REOM^3 results reproduce the experimentally-determined enhancement of the cross section at 7.5 MeV. Furthermore, when comparing the REOM^3 cross sections obtained with a 50 keV smearing parameter and the average elastic cross sections deduced in 50 keV steps (Panel (c)), a good agreement in the strength fragmentation can be observed up to 8.5 MeV. At higher energies, the energies of the enhancements cannot exactly be reproduced but similar structures can be identified. Here, the inelastic contribution is not included since it could not be extracted in 50 keV steps and, therefore, no fine structure could be investigated.

The agreement of REOM^3 with experimental data, although improved compared to the less advanced approaches, is still imperfect. Especially, the summed cross section between 6.0 and 9.3 MeV is almost two times higher than the experimentally extracted upper limit of the total photoabsorption cross section (dark-red data points) as illustrated in Fig. 9. This indicates that some mechanisms of the strength formation are still to be included to achieve spectroscopic accuracy, and that the interaction can be of better quality. In the paradigm of a parameter-free many-body theory, the only parameters are those characterizing the local interaction between two nucleons (effective or bare), while all the many-body correlations are computed without changing these parameters or introducing new ones.

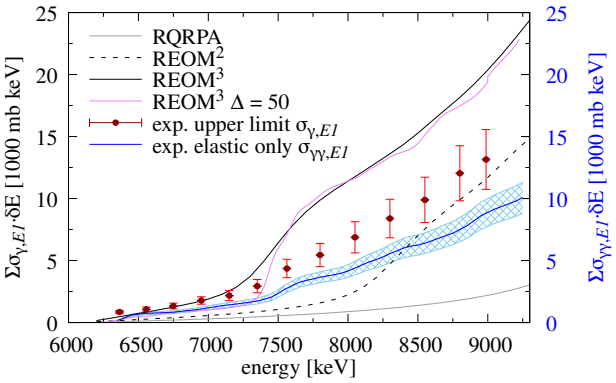

FIG. 9. The running sums of the $E1$ photoabsorption cross sections $\Sigma\sigma_{\gamma,E1}$ of ^{64}Ni deduced from RQRPA (gray), REOM^2 (dashed black), and REOM^3 calculations are depicted. In the case of the REOM^3, the result using a smearing parameter of $\Delta = 200$ keV is shown as a black solid curve, and the $\Delta = 50$ keV calculation as a purple solid one. The running sums of the experimentally-deduced upper limit for the total photoabsorption cross section of the $E1$ contribution and the corresponding statistical uncertainties are depicted in dark red. The systematic uncertainties are shown in lighter red. The running sum of the experimental NRF elastic cross section $\sigma_{\gamma\gamma,E1}$ is illustrated in blue (systematic uncertainties as light-blue crosshatched areas) with the corresponding y axis on the right side.

Within this paradigm, a complete response theory for atomic nuclei should take into account the continuum, including the multiparticle escape, a more complete set of phonons (including those of unnatural parity and isospin-flip), complex ground-state correlations, and, in principle, even higher-complexity configurations, which are expected to further affect the strength functions and potentially improve the description of the fine structure. These factors may be individually less significant than the included correlations but altogether they can make a sizable contribution. These effects will be addressed in future work.

For a better comparison, the contribution of the inelastic-decay channel in the experiment has to be further investigated with respect to the contributions of $E1$ and $M1$ transitions. Furthermore, the deduced average inelastic cross sections serve only as an estimate of the inelastic-decay channel, since the non-constant photon-current densities were neglected in the analysis. By analyzing $\gamma-\gamma$ coincidence data, a smaller energy region δE can be investigated similar to that used for the average elastic cross section.

V.2. Shell-model calculations

Shell-model calculations for ^{64}Ni were carried out using the code NuShellX@MSU [62] with two different model spaces.

First, the fp model space with the GX1A Hamiltonian [63, 64] was used as previously for the lighter nuclide ^{54}Fe [19]. The model space included the proton and neutron orbitals $(1f_{7/2}, 2p_{3/2}, 1f_{5/2}, 2p_{1/2})$ without limits in occupation numbers. The calculated 2^+_1 state has an excitation energy of $E_x = 1.268$ MeV and a transition strength to the ground state of $B(E2, 2^+_1 \rightarrow 0^+_1) = 139\, e^2\text{fm}^4$. The corresponding experimental values are $E_x = 1.346$ MeV and $B(E2, 2^+_1 \rightarrow 0^+_1) = 119(4)\, e^2\text{fm}^4$ [50].

As an alternative, the ca48pn model space with the CA48MH1 Hamiltonian [65, 66] was applied, which had also been used for the investigation of 1^+ states in the isotone ^{66}Zn [24] and in ^{60,64,68}Fe [67]. The model space included the $\pi(1f_{7/2}^{(8-f)}, 1f_{5/2}^{f}, 2p_{3/2}^{f}, 2p_{1/2}^{p1})$ proton orbitals with $f = 0$ to 4, $p1 = 0$ to 2, and the $\nu(1f_{5/2}^{f5}, 2p_{3/2}^{p3}, 2p_{1/2}^{p1}, 1g_{9/2}^{g9})$ neutron orbitals, where $f5$ and $p3$ can have values from zero to the respective maximum, and $g9 = 0$ to 2. The 2^+_1 state was calculated at $E_x = 0.750$ MeV with a transition strength of $B(E2, 2^+_1 \rightarrow 0^+_1) = 423\, e^2\text{fm}^4$ using standard effective charges of $e_\pi = 1.5e$ and $e_\nu = 0.5e$. It is noted that the Hamiltonians were not specifically adjusted to nuclides around ^{64}Ni. The calculations for $J^\pi = 1^+$ states were performed for the lowest 100 states. Reduced transition strengths $B(M1, 1^+ \rightarrow 0^+_1)$ were calculated using effective g factors of $g_s^{\text{eff}} = 0.74 g_s^{\text{free}}$ [68].

The experimentally deduced products of $B(M1, 1^+ \rightarrow 0^+_1)$ and the ground-state decay branching ratio Γ_0/Γ given in Table I for all firm and possible 1^+ states are compared with the calculated ones in Fig. 10. The first 1^+ state in the shell-model calculation using the CA48MH1 (GX1A) Hamiltonian appears at 2.941 (2.692 MeV), whereas the first experimental state with a firm 1^+ assignment is located at 4.617(1) MeV. However, excitation energies below 4.33 MeV were not covered by the HIγS measurement. Therefore, the lowest-lying calculated 1^+ states within the shell model are not given in the figure.

Around 8 MeV, an accumulation of strong $M1$ transitions and a number of transitions with smaller $B(M1)$ values above 8.5 MeV are observed in the experiment (upper part of Fig. 10). This resembles the distribution calculated with the GX1A Hamiltonian (black bars in the lower panel). The shell-model results obtained with the CA48MH1 Hamiltonian show prominent strengths between 7 and 7.5 MeV and also a distribution of smaller strengths at higher energy (red bars in the lower panel). This behavior is also indicated in the running sums calculated using all values above 4 MeV determined theoretically and experimentally (cf. Fig. 11). The experimental running sum includes all firmly assigned as well as all possible $M1$ transitions observed in the NRF experiments. All the curves indicate a step-like behavior caused by strong peaks in the $B(M1)$ distributions. Whereas the steepest step occurs between 7.5 and 8 MeV in the experimental (orange) and the GX1A (black) data, the CA48MH1 results (red) contain two steep steps at 7 and 7.5 MeV. Because of these two steps, the running sums in CA48MH1 exceed the experimental ones as well as those calculated in GX1A above 7 MeV, but approach the experimental values again at 8.5 MeV. Additionally, it is

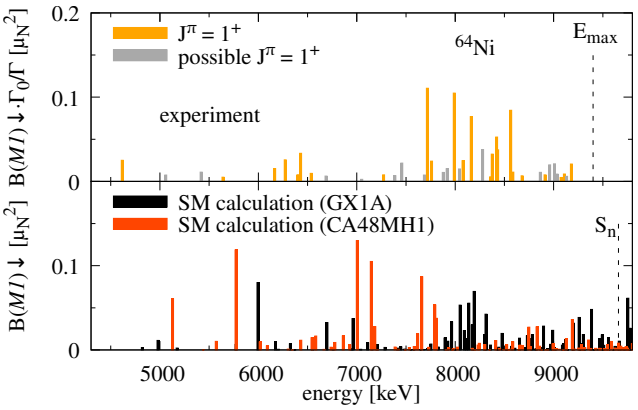

FIG. 10. Upper panel: The products of experimental $B(M1, 1^+ \rightarrow 0_1^+)$ and the ground-state decay branching ratio Γ_0/Γ are illustrated for all firmly identified $M1$ transitions as orange bars and for all transitions with unknown radiation character as gray bars. The maximum energy, for which absolute values could experimentally be determined, is indicated by a dashed vertical line. Lower panel: $B(M1, 1^+ \rightarrow 0_1^+)$ values for the lowest 100 1^+ states deduced by the shell-model calculations using, on the one hand, the CA48MH1 Hamiltonian and, on the other, the GX1A Hamiltonian are shown as red and black bars, respectively. Here, the neutron-separation threshold of ^{64}Ni is indicated by a dashed vertical line.

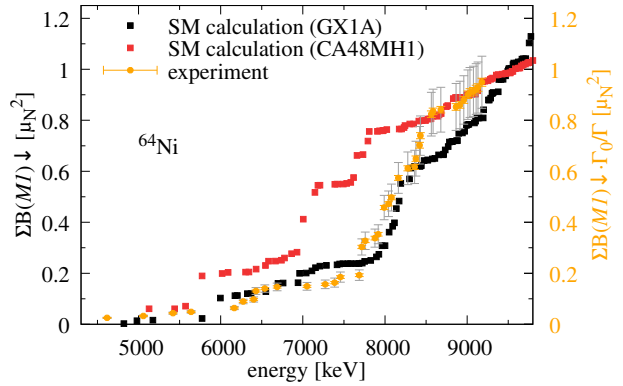

FIG. 11. Running sums $\sum B(M1, 1^+ \rightarrow 0_1^+)$ of the calculated values using the CA48MH1 and GX1A Hamiltonian are shown as red and black squares, respectively. The experimentally extracted products of $B(M1, 1^+ \rightarrow 0_1^+)$ and ground-state decay branching ratio Γ_0/Γ (right y axis) of ^{64}Ni are given by orange circles with the corresponding statistical uncertainties. The systematic uncertainties are depicted in gray.

indicated that the strength in the GX1A shell-model calculations is more smoothly distributed compared to the experimental strength between approximately 8.5 MeV and 9.5 MeV. The differences between the distributions of $M1$ strength obtained with the two model spaces may be traced back to differences in the ingredients, such as single-particle energies and two-body matrix elements. The calculation using GX1A without limitations reproduces the energy of the 2_1^+ state and the $B(E2, 2_1^+ \rightarrow 0_1^+)$ value better than the one using CA48MH1, which may indicate a better adjustment of model space and Hamiltonian to the present nuclide. In both model spaces, the excitation of protons from the $1f_{7/2}$ orbital to the fp orbitals across the $Z = 28$ gap plays an important role for the generation of $M1$ strength. In GX1A, also the neutron $1f_{7/2}$ orbital is included while CA48MH1 starts above $N = 28$, but includes the $1g9/2$ orbital in addition. Both these orbitals give minor contributions to the respective calculated states, but may nevertheless influence the results in different ways.

It has to be kept in mind that the experimental data are given as the product of the reduced transition strength and the ground-state decay branching ratio. In this sense, the pictured experimental values serve only as upper limit. On the other hand, only resolved transitions are contained in the experimental data.

It can be concluded that the experimental summed strength of $\Sigma B(M1, 1^+ \rightarrow 0_1^+) = 0.949(16)(102)\mu_N^2$ between 4.3 and 9.3 MeV is well reproduced by both shell-model calculations which amount to $\Sigma B(M1, 1^+ \rightarrow 0_1^+) = 0.96\mu_N^2$ using the CA48MH1 Hamiltonian and to $\Sigma B(M1, 1^+ \rightarrow 0_1^+) = 0.89\mu_N^2$ with the GX1A Hamiltonian. The summed strength is very similar to that of the neutron-magic ($N = 28$) ^{54}Fe [19] and almost three times larger than that of the $N = 36$ isotone ^{66}Zn [24] up to 9.3 MeV. This increase is expected because proton excitations across $Z = 28$ play an important role for $M1$ excitations of ^{64}Ni, whereas this contribution is small for ^{66}Zn, which already has two protons above the $Z = 28$ shell closure.

VI. SUMMARY AND OUTLOOK

Real-photon scattering experiments on ^{64}Ni were performed using both an energetically-continuous, mainly unpolarized (bremsstrahlung) photon beam and a quasi-monoenergetic, linearly-polarized γ-ray beam. This combination enabled the firm (tentative) identification of 87 (8) $E1$, 23 (2) $M1$, and 11 dipole transitions of unknown radiation character between 4.3 MeV and 9.7 MeV. For 11 observed transitions, neither the multipole order nor the radiation character could be firmly assigned. Because of the use of a calibration standard during the bremsstrahlung experiment, absolute energy-integrated cross sections of transitions up to 9.3 MeV were deduced by combining both experiments. In addition to the analysis of individual transitions, average elastic cross sections $\sigma_{\gamma\gamma}$ were determined up to 9.2 MeV. The contributions of the $E1$ and $M1$ channel with respect to the total elastic cross section were calculated up to the neutron-separation energy $S_n = 9.7$ MeV of ^{64}Ni. It was observed that the $E1$ contribution is, in general, larger than the $M1$ contribution although an accumulation of $M1$ transitions was observed between 7.5 and 8.5 MeV.

Shell-model calculations were performed using two different Hamiltonians (CA48MH1 and GX1A). The resulting reduced $M1$ transition strengths $B(M1, 1^+ \rightarrow 0_1^+)$ were compared to the experimentally deduced products

of reduced transition strength and ground-state decay branching ratio $B(M1, 1^+ \rightarrow 0_1^+) \cdot \Gamma_0/\Gamma$ of individual transitions. Although, the agreement of the summed strength between 4.3 and 9.3 MeV is good for both calculations with respect to the experimental value, the fine structure, i.e., an accumulation of strength between 7.5 and 8.5 MeV, is better reproduced by the shell-model calculation carried out in the fp model space with the GX1A Hamiltonian. The experimental summed strength is very similar to that of the neutron-magic $N = 28$ nucleus ^{54}Fe [19] and almost three times larger than that of the $N = 36$ isotone ^{66}Zn [24] up to 9.3 MeV. Also, the calculated $M1$ strength of ^{64}Ni exceeds the one of ^{66}Zn by about 50 %. Large $M1$ strengths are attributed to proton excitations across the $Z = 28$ gap, including holes in the $1f_{7/2}$ orbital. These play an important role for excited 1^+ states of ^{64}Ni, whereas their contributions to states in ^{66}Zn, which already has two protons above the $Z = 28$ shell closure, are smaller.

The average elastic cross section of the $E1$ channel and an upper limit of the total photoabsorption cross section, including decays to states other than the ground state, were compared to calculations in the relativistic equation of motion REOM framework including $2q \otimes phonon$ REOM^2 and $2q \otimes 2phonon$ REOM^3 configurations. It was found that the inclusion of more complex configurations leads to a lowering of the energy of a significant part of the $E1$ strength. The $E1$ part of the photoabsorption cross sections $\sigma_{\gamma,E1}$ extracted from the calculations were compared to the NRF results. It was observed that the REOM^3 calculation describes the gross structures of the average elastic cross section well, i.e., enhancements of the cross section up to approximately 8.5 MeV. At higher energies, the energies of the enhancements are not as well described, but nevertheless, similar structures can be observed. Besides the good reproduction of the cross section's behavior, the absolute value of the REOM^3 calculation is approximately two times larger than the experimental value. Possible reasons for this discrepancy can be found on both the experimental and theoretical sides. On the one hand, for the estimate of the average inelastic cross section, the non-constant photon distribution was neglected. This can be taken into account by investigating $\gamma - \gamma$ coincidence data, and extracting the inelastic cross section in smaller energy steps than it was done for the elastic cross section. On the other hand, more mechanisms contributing to the strength formation have to be included in the theory for a better description of the experimental data.

For both radiation characters, the missing exact knowledge of the inelastic decay channel makes comparisons to theory difficult. Furthermore, a remeasurement at energies between 9.3 MeV and S_n is important for conclusive comparisons to, e.g., the (γ, n) data by Utsonomiya *et al.* [60] with respect to a possible enhancement of $E1$ strength on top of the low-energy tail of the IVGDR in the PDR region.

ACKNOWLEDGEMENT

The authors thank the accelerator staff at HIγS and γELBE for providing excellent photon beams and A. Hartmann for the technical assistence. The work of E.L. was supported by the GANIL Visitor Program, US-NSF Grant PHY-2209376, and US-NSF Career Grant PHY-1654379. R.S. thanks B. A. Brown for his support in using the code NUSHELLX@MSU and gratefully acknowledges the allocation of computing time through the Centers for High-Performance Computing of Helmholtz-Zentrum Dresden-Rossendorf and of Technische Universität Dresden. The members of the UWS Nuclear Physics Research Group acknowledge financial support from the UK Science and Technology Facilities Council (STFC, Grant No. ST/P005101/1). This work was supported in part by the U.S. Department of Energy, Office of Nuclear Physics under grant numbers DE-FG02-97ER41033 (Duke University) and DE-FG02-97ER41041 (UNC). J.I. and O.P. are supported by the Deutsche Forschungsgemeinschaft (DFG, German Research Foundation) – Project-ID 279384907 – SFB1245 and by the grant "Nuclear Photonics" within the LOEWE program of the State of Hesse. J.I. acknowledges the support by the State of Hesse within the Research Cluster ELEMENTS (Project ID No. 500/10.006). This work was supported by the BMBF (05P21PKEN9).

[1] M. Harakeh and A. van der Woude, *Giant Resonances* (Oxford University Press, 2001).
[2] D. Savran, T. Aumann, and A. Zilges, Prog. Part. Nucl. Phys. **70**, 210 (2013).
[3] A. Bracco, E. Lanza, and A. Tamii, Prog. Part. Nucl. Phys. **106**, 360 (2019).
[4] E. Lanza, L. Pellegri, A. Vitturi, and M. Andrés, Progress in Particle and Nuclear Physics **129**, 104006 (2023).
[5] D. Savran, M. Fritzsche, J. Hasper, K. Lindenberg, S. Müller, V. Y. Ponomarev, K. Sonnabend, and A. Zilges, Phys. Rev. Lett. **100**, 232501 (2008).
[6] A. P. Tonchev, S. L. Hammond, J. H. Kelley, E. Kwan, H. Lenske, G. Rusev, W. Tornow, and N. Tsoneva, Phys. Rev. Lett. **104**, 072501 (2010).
[7] R.-D. Herzberg *et al.*, Phys. Lett. B **90**, 49 (1997).
[8] B. Löher *et al.*, Phys. Lett. B **756**, 72 (2016).
[9] A. Zilges, S. Volz, M. Babilon, and P. Mohr, Phys. Lett. B **542**, 43 (2002).
[10] S. Volz, N. Tsoneva, M. Babilon, and M. Elvers, Nuclear Phys. A **779**, 1 (2006).
[11] D. Savran *et al.*, Phys. Rev. C **84**, 024326 (2011).
[12] K. Govaert, F. Bauwens, J. Bryssinck, D. De Frenne, E. Jacobs, W. Mondelaers, L. Govor, and V. Y. Ponomarev, Phys. Rev. C **57**, 2229 (1998).
[13] F. Schlüter, private communication.
[14] J. Endres *et al.*, Phys. Rev. C **85**, 064331 (2012).
[15] B. Özel-Tashenov *et al.*, Phys. Rev. C **90**, 024304 (2014).
[16] M. Müscher *et al.*, Phys. Rev. C **102**, 014317 (2020).

[17] M. Weinert, M. Spieker, G. Potel, N. Tsoneva, M. Müscher, J. Wilhelmy, and A. Zilges, Phys. Rev. Lett. **127**, 242501 (2021).
[18] D. Savran *et al.*, Physics Letters B **786**, 16 (2018).
[19] R. Schwengner *et al.*, Phys. Rev. C **101**, 064303 (2020).
[20] T. Shizuma, T. Hayakawa, H. Ohgaki, H. Toyokawa, T. Komatsubara, N. Kikuzawa, T. Inakura, M. Honma, and H. Nakada, Phys. Rev. C **87**, 024301 (2013).
[21] F. Bauwens, J. Bryssinck, D. De Frenne, K. Govaert, L. Govor, M. Hagemann, J. Heyse, E. Jacobs, W. Mondelaers, and V. Y. Ponomarev, Phys. Rev. C **62**, 024302 (2000).
[22] M. Scheck *et al.*, Phys. Rev. C **87**, 051304 (2013).
[23] M. Scheck *et al.*, Phys. Rev. C **88**, 044304 (2013).
[24] R. Schwengner *et al.*, Phys. Rev. C **103**, 024312 (2021).
[25] D. Savran *et al.*, Phys. Rev. C **106**, 044324 (2022).
[26] F. R. Metzger, Prog. Nucl. Phys. **7**, 53 (1959).
[27] U. Kneissl, H. Pitz, and A. Zilges, Progress in Particle and Nuclear Physics **37**, 349 (1996).
[28] A. Zilges, D. Balabanski, J. Isaak, and N. Pietralla, Progress in Particle and Nuclear Physics **122**, 103903 (2022).
[29] N. Pietralla *et al.*, Phys. Rev. Lett. **88**, 012502 (2001).
[30] C. Romig *et al.*, Phys. Rev. C **88**, 044331 (2013).
[31] J. Isaak *et al.*, Physics Letters B **727**, 361 (2013).
[32] R. Schwengner *et al.*, Nucl. Instrum. Methods Phys. Res., Sect. A **555**, 211 (2005).
[33] H. R. Weller, M. W. Ahmed, H. Gao, W. Tornow, Y. K. Wu, M. Gai, and R. Miskimen, Prog. Part. Nucl. Phys. **62**, 257 (2009).
[34] B. Löher *et al.*, Nucl. Instrum. Methods Phys. Res., Sect. A **723**, 136 (2013).
[35] S. Agostinelli *et al.*, Nucl. Instrum. Methods Phys. Res., Sect. A **506**, 250 (2003).
[36] J. Allison *et al.*, IEEE Trans. Nucl. Sci. **53**, 270 (2006).
[37] J. Allison *et al.*, Nucl. Instrum. Methods Phys. Res., Sect. A **835**, 186 (2016).
[38] R. Massarczyk *et al.*, Phys. Rev. C **86**, 014319 (2012).
[39] U. Friman-Gayer, J. Kleeman, and O. Papst, `https://github.com/uga-uga/utr` (2022).
[40] E. Haug, Radiation Physics and Chemistry **77**, 207 (2008).
[41] G. Roche, C. Ducos, and J. Proriol, Phys. Rev. A **5**, 2403 (1972).
[42] F. Salvat, J. D. Martˇnez, R. Mayol, and J. Parellada, Phys. Rev. A **36**, 467 (1987).
[43] F. Ajzenberg-Selove, Nucl. Phys. A **506**, 1 (1990).
[44] G. Rusev, A. P. Tonchev, R. Schwengner, C. Sun, W. Tornow, and Y. K. Wu, Phys. Rev. C **79**, 047601 (2009).
[45] J. Isaak *et al.*, Phys. Rev. C **103**, 044317 (2021).
[46] U. Friman-Gayer, J. Kleeman, and O. Papst, `https://github.com/uga-uga/Horst` (2022).
[47] Y. Wu, personal communication (2022).
[48] C. Sun and Y. K. Wu, Phys. Rev. ST Accel. Beams **14**, 044701 (2011).
[49] M. Tamkas *et al.*, Nuclear Physics A **987**, 79 (2019).
[50] B. Singh and J. Chen, Nucl. Data Sheets **178**, 42 (2021).
[51] S. Adachi and P. Schuck, Nuclear Physics A **496**, 485 (1989).
[52] J. Dukelsky, G. Röpke, and P. Schuck, Nuclear Physics A **628**, 17 (1998).
[53] D. J. Rowe, Rev. Mod. Phys. **40**, 153 (1968).
[54] E. Litvinova and P. Schuck, Phys. Rev. C **100**, 064320 (2019).
[55] E. Litvinova and Y. Zhang, Phys. Rev. C **106**, 064316 (2022).
[56] V. I. Tselyaev, Phys. Rev. C **88**, 054301 (2013).
[57] G. Lalazissis, S. Karatzikos, R. Fossion, D. P. Arteaga, A. Afanasjev, and P. Ring, Physics Letters B **671**, 36 (2009).
[58] S. E. Agbemava, A. V. Afanasjev, D. Ray, and P. Ring, Phys. Rev. C **89**, 054320 (2014).
[59] E. Litvinova, arXiv:2308.07574.
[60] H. Utsunomiya *et al.*, Phys. Rev. C **98**, 054619 (2018).
[61] M. Q. Hlatshwayo, J. Novak, and E. Litvinova, Phys. Rev. C **109**, 014306 (2024).
[62] B. Brown and W. Rae, Nuclear Data Sheets **120**, 115 (2014).
[63] M. Honma, T. Otsuka, B. A. Brown, and T. Mizusaki, Phys. Rev. C **69**, 034335 (2004).
[64] M. Honma, T. Otsuka, B. A. Brown, and T. Mizusaki, , Eur. Phys. J. A **25**, 499 (2005).
[65] M. Hjorth-Jensen, T. T. Kuo, and E. Osnes, Physics Reports **261**, 125 (1995).
[66] M. Hjorth-Jensen, personal communication.
[67] R. Schwengner, S. Frauendorf, and B. A. Brown, Phys. Rev. Lett. **118**, 092502 (2017).
[68] M. Honma, T. Otsuka, T. Mizusaki, M. Hjorth-Jensen, and B. A. Brown, Journal of Physics: Conference Series **20**, 7 (2005).